Nanoscale

Accepted Manuscript

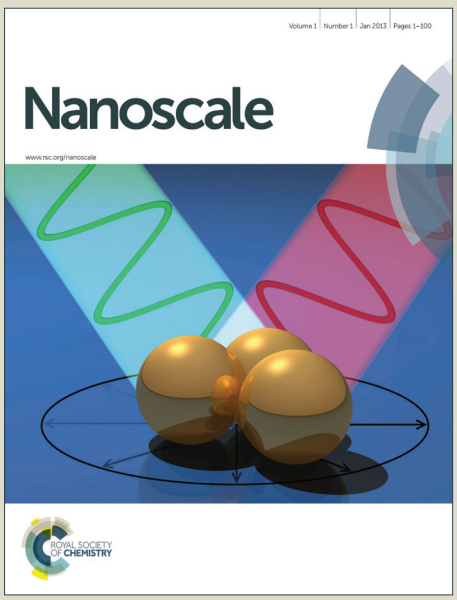

ROYAL SOCIETY OF CHEMISTRY

www.rsc.org/nanoscale

Nanoscale

RSCPublishing

ARTICLE

Synthesis of nitrogen-doped activated graphene aerogel/gold nanoparticle and its application for electrochemical detection of hydroquinone and o-dihydroxybenzene

Cite this: DOI: 10.1039/x0xx00000x

Received 00th January 2012,
Accepted 00th January 2012

DOI: 10.1039/x0xx00000x

www.rsc.org/

Zhang Juanjuan,[a] Li Ruiyi,[b] Li Zaijun,[a,c*] Liu Junkang,[a] Gu Zhiguo[a] and Wang Guangli[a]

Graphene aerogel materials have attracted increasing attention owing to their large specific surface area, high conductivity and electronic interactions. Here, we for the first time reported a novel strategy for synthesis of nitrogen-doped activated graphene aerogel/gold nanoparticles (N-doped AGA/GNs). First, the mixture of graphite oxide, 2,4,6-trihydroxybenzaldehyde, urea and potassium hydroxide was dispersed in water and subsequently heated to form graphene oxide hydrogel. Then, the hydrogel was dried by freeze-drying and reduced by thermal annealing in Ar/H_2 environment in sequence. Finally, GNs were adsorbed on the surface of N-doped AGA. The resulting N-doped AGA/GNs offers excellent electronic conductivity (2.8×10^3 S m^{-1}), specific surface area (1258 m^2 g^{-1}), well-defined 3D hierarchical porous structure and apparent heterogeneous electron transfer rate constant (40.78±0.15 cm s^{-1}), which are remarkably better than that of present graphene aerogel materials. Moreover, N-doped AGA/GNs was used as a new sensing material for electrochemical detection of hydroquinone (HQ) and o-dihydroxybenzene (DHB). Owing to the greatly enhanced electron transfer and mass transport, the sensor displays ultrasensitive electrochemical response to HQ and DHB. Its differential pulse voltammetric peak current linearly increases with the increase of HQ and DHB in the range of 5.0×10^{-8}□1.8×10^{-4} M for HQ and 1×10^{-8}□2.0×10^{-4} M for DHB. The detection limit is 1.5×10^{-8} M for HQ and 3.3×10^{-9} M for DHB (S/N=3). The method provides the advantage of sensitivity, repeatability and stability compared with present HQ and DHB sensors. It has been successfully applied to detection of HQ and DHB in real water samples with the spiked recovery in the range of 96.8-103.2%. The study also provides a promising approach for the fabrication of various graphene aerogel materials with improved electrochemical performances, which can be potentially applied in biosensor, electrocatalysis, and energy storage/conversion devices.

1 Introduction

Graphene aerogel is a mesoporous structure formed by three-dimensional interconnected graphene sheets. Compared with the porous graphene materials constructed by physically and randomly stacked graphene sheets, graphene aerogel possesses much higher electronic conductivity since the constituent graphene sheets are chemically bonded, facilitating much faster charge transport across graphene sheet junctions, high specific surface area that offers abundant active sites for the catalytic reduction events, and large pore volume that provides fast mass transfer of the redox species.[1] To meet the need of different application, graphene oxide also combines with the chemical reagent containing special groups or structure such as DNA,[2] poly(vinyl alcohol)[3] and polyamines[4] and nanoparticles[5] to create multifunctional graphene aerogel. To date, graphene-based aerogel materials have attracted increasing attention and demonstrated potential applications in many fields, including supercapacitors,[6] lithium-ion battery,[7] ethanol fuel cells,[8] adsorbing materials for Cu^{2+}, crude oil[9] and acetone gas,[10] phase change materials for thermal management[11] and sensing.[12]

Many efforts have attempted to improve synthesis of graphene aerogel and fabricate graphene hybrid in the recent years. The procedure for synthesis of graphene aerogel typically includes self-assembly of graphene oxide, drying and reduction of graphene oxide hydrogel. The hydrothermal method was an important approach for creating three-dimensional macroporous graphene architecture. During the hydrothermal treatment, the partially reduced graphene oxide was coalesced and formed strong a cross-links of three-dimensional graphene network with the assistance of van der Waals' forces, p-p stacking and abundant hydrogen bonds of water. However, conventional hydrothermal process is time-consuming and energy-consuming, and the resulting aerogel lacks of enough

mechanical strength. In view of the above problems, the first solution is to use chemical reducing agent to reduce the raection temperature and time. Xing et al. reported synthesis of the graphene aerogel through simultaneous self-assembly and reduction with hypophosphorous acid and I_2 as the reductants.[13] The reaction temperature and time are reduced to 90℃ and 12 h, respectively. The graphene aerogel could reach as high as special surface area of 830 m^2 g^{-1}. The second solution is to use special crosslinking agent to enhance the mechanical strength of graphene aerogel. Liu et al. reported a tri-isocyanate reinforced graphene aerogel and its application in crude oil adsorption.[14] Tri-isocyanate formed a conformal coating over the surface of three-dimensional framework, serving to reinforce the framework by widening the neck regions between neighboring nanoparticles. The graphene aerogel gives low bulk density, high compressive failure strength, and good adsorption ability towards crude oil. In the drying step, high mechanical strength of the graphene oxide hydrogel will be completely destroyed by classical drying, because of the loss of hydrogen bonds. However, the use of lower freezing point and slow drying technologies can effectively overcome the structural damage during the drying of graphene oxide hydrogel. The lower freezing point method is to add some special chemical reagents such as ammonia into graphene oxide solution to lower freezing point to below zero. The method can retard freezing and keep original structure. Moreover, the reaction between the chemical reagent and the graphene oxide may bring some covalent bonds among graphene sheets, which could enhance the mechanical strength of graphene aerogel. The slow drying is to use special drying technology such as freeze-drying and supercritical CO_2 drying to reduce structural damage of the graphene aerogel by prolonging the drying time. Wu et al. reported synthesis of the graphene aerogel by the self-assembly of graphene oxide at low temperature, followed by supercritical CO_2 drying and H_2 reduction at high temperature. The graphene aerogel shows high specific surface area. The supercritical CO_2 drying method effectively prevent the restacking of reduced graphene sheets, resulting in three-dimensional graphene materials with large specific surface area.[15] In the reduction step, the reduction degree of graphene oxide is very important to electronic conductivity of the graphene materials. Up to now, the thermal annealing in Ar/H_2 is one of the most efficient approach for the reduction of graphene oxide.[16] Except for the synthesis of three-dimensional graphene materials, the construction of graphene hybrids has become another hot research. The integration of nanomaterials on graphene paves a new way to enhance electronic, chemical, and electrochemical properties of graphene materials.[17,18] Cao et al. reported a new method to grow gold and other metal clusters on the reduced graphene oxide sheets in the absence of any additional protecting molecule and reductant.[19] The experiment result shows that the strong absorption and the moderate reduction of the reduced graphene oxide toward metal ions in the solution are the key for providing the initial nuclear sites and restraining the growth of gold clusters. The gold cluster/graphene hybrid displays an impressive eletrocatalytic performance toward oxygen reduction reaction, for instance, high onset potential, superior methanol tolerance, and excellent stability. Cheng et al. reported an ultra tough artificial nacre based on the graphene oxide sheets by conjugated cross-linking.[20] Highly p-conjugated long-chain polymers made of 10,12-pentacosadiyn-1-ol monomers are cross-linked with the graphene oxide sheets, resulting in a huge displacement upon loading and adsorption of much more fracture energy. The toughness is two higher than that of the natural nacre. Though much progress has been made, present graphene aerogel materials also lack the desired electrochemical properties for their applications in some fields such as sensing and supercapacitors. There is a great need to develop new strategy for building up graphene aerogel hybrids with excellent electronic conductivity and well-defined three-dimensional hierarchical porous structure.

The study focuses on the synthesis of nitrogen-doped activated graphene aerogel/gold nanoparticles (N-doped AGA/GNs) and its application for electrochemical detection of hydroquinone (HQ) and o-dihydroxybenzene (DHB). The resulting N-doped AGA/GNs offers excellent electronic conductivity, large specific surface area, well-defined three-dimensional hierarchical porous structure and fast apparent heterogeneous electron transfer. Owing to the largely enhanced electrochemical behavior and electrocatalytic activity towards HQ and DHB, the sensor based on the N-doped AGA/GNs presents an advantage of sensitivity, repeatability and stability compared with present HQ and DHB sensors.

2 Experimental

2.1 Materials and reagents

Graphite, chlorauric acid ($HAuCl_4$), potassium hydroxide (KOH), hydroquinone (HQ), o-dihydroxybenzene (DHB), resorcrinol (RC) and 2,4,6-trihydroxybenzaldehyde were purchased from Sigma-Aldrich Chemical Company (Mainland, China) and used without further purification. Graphite oxide (GO) was prepared from natural graphite by Hummers' method.[21] Phosphate-buffered saline (PBS, pH 7.0, Na_2HPO_4-KH_2PO_4-NaCl-KCl, 0.01 M) was prepared in the laboratory. The chitosan solution was prepared by dissolving 5.0 g of chitosan in 100 ml of 1.0% (v/v) acetic acid. All other reagents employed were of analytical reagent grade or with highest quality and were purchased from Shanghai Chemical Company (Shanghai, China). Ultra pure water (18.2 MΩ cm) purified from a Milli-Q purification system was used throughout the experiment.

2.2 Synthesis of GNs

A 1.0 ml of $HAuCl_4$ solution (5 mM) was added into 50 ml of ultrapure water. After the solution was heated to 100°C, 2.5 ml of tri-sodium citrate solution (3.4 nM) was rapidly injected under vigorous stirring (500 rpm). The solution was refluxed at 100°C for 1 h, then cooled to ambient temperature, and finally filtered using a cellulose acetate membrane with the bore diameter of 0.26 to obtain a GN solution.

2.3 Preparation of N-doped AGA/GNs

The preparation of N-doped AGA/GNs includes four assemble processes, i.e. the self-assembly of GO sheets, freeze-drying of

GO hydrogel, thermal annealing of GO aerogel and hybridization of N-doped AGA with GNs. (1) A 300 mg of graphite oxide was dispersed in 100 ml of 1 M KOH solution by ultrasonication to form homogeneous GO dispersion. A 2 g of urea and 50 mg of 2,4,6-trihydroxybenzaldehyde were added to the dispersion with magnetic stirring for several minutes until completely dissolving. Then, the mixed solution was transferred into a 500 ml of autoclave pressure vessel and then heated for 6 h at 90℃. During this time, GO sheets will self-assemble into GO hydrogel. (2) The hydrogel was dried by freeze-drying for 48 h at -50℃ to form GO aerogel. (3) The aerogel was reduced by thermal treatment in Ar/H_2 (v:v=95:5) environment for 4 h at 850℃ to obtain N-doped AGA. Then, the sample was washed to neutral with distilled water and dried for 12 h in vacuum at 50℃. (4) The dried N-doped AGA was immersed in the GN solution. After all of the GN solution was sucked into the N-doped AGA, the hybrid was subjected to dry by freeze-drying at -50℃ for 12 h.

2.4 General characterization

Electrical conductivity measurements were carried out in a ST-2258C multifunction digital four-probe tester which equipped with a SZT-D semiconductor powder resistivity tester (Suzhou Jingge Electronic Co., Ltd., China). The powder sample was directly placed in a round hole with the diameter of 5 mm on the SZT-D semiconductor powder resistivity tester. Then, the powder was slowly compressed by the piston on the system. At the same time, the electrical conductivity values under different pressures were automatically recorded. Scanning electron microscope (SEM) analysis was carried out in a HITACHI S4800 field emission scanning electron microscope. SEM sample was prepared by placing a drop of dilute ethanol dispersion of the composites onto a copper plate attached to an aluminum sample holder, and the solvent was allowed to evaporate at room temperature. Transmission electron microscope (TEM) analysis was conducted on a JEOL 2010 transmission electron microscope at 200 keV. The sample was prepared by dispensing a small amount of dry powder in ethanol. Then, one drop of the suspension was dropped on 300 mesh copper. TEM grids covered with thin amorphous carbon films. X-ray diffraction (XRD) patterns were measured on a X-ray D8 Advance Instrument operated at 40 kV and 20 mA and using Cu Kα radiation source with λ=0.15406 nm. Infrared spectrum (IR) was recorded on a Nicolet FT-IR 6700 spectrometer. Raman measurements were carried out using a InVia laser micro-Raman spectrometer. X-ray photoelectron spectroscopy (XPS) measurements were performed using a PHI 5700 ESCA spectrometer with monochromated Al KR radiation (hv=1486.6 eV). The N_2 adsorption and desorption isotherms were measured at 77 K on a Quantachrome Nova 2000 and the CO_2 isotherms were recorded at 273 K with a Micromeritics TriStar 3000. Prior to the gas sorption measurements, all the samples were outgassed in vacuum at 120°C for 24 h. The specific surface area and the pore size distribution were calculated using the Braunauer-Emmett-Teller (BET) method and the relative pressure range of p/p_0 from 0.1 to 0.3 was used for multipoint BET calculations. Non-local density functional theory (NLDFT) assuming the pores are slit/cylinder shaped was used to determine the pore size distribution and mesopore volume. PerkinElmer PE 2400 Elemental Analyzer was used for the determination of carbon, oxygen and nitrogen in various graphene materials. SpectrAA 220Z Atomic Absorption Spectrometer was used for gold analysis, in which the sample was digested by aqua regia in advance.

2.5 Electrochemical measurements

Electrochemical experiments were performed with an CHI660D electrochemical workstation (Shanghai, China). Conventional three electrode system was used for cyclic voltammetry (CV) and differential pulse voltammetry (DPV) with Ag/AgCl (saturated KCl) electrode as the reference electrode, platinum wire as the counter electrode, and bare or modified glassy carbon electrode (GCE, 1.0 mm in diameter) as the working electrode. Before use, GCE was polished successively with 1.0, 0.3, and 0.05 μm alumina powder, and sonicated in a 6.0 M of nitric acid/doubly distilled water and ethanol/doubly distilled water for 20 min. Then, the GCE as working electrode was subjected to cyclic scanning in 0.5 M of sulphuric acid solution in a potential range from -0.1 V to 1.0 V. When the cyclic voltammogram was almost unchanged, the electrode was taken out, cleaned with ultra pure water and dried in a stream of nitrogen. The treated GCE was modified with different graphene material to prepare different sensor using the following procedure: the N-doped AGA/GNs (or other graphene materials) was dissolved in ethyl acetate to make up 0.2 mg ml^{-1} solution, then 10 μl mixture was dropped on the surface of GCE, after that 2 μl of chitosan solution was carefully spreading on the as-prepared N-doped AGA/GNs surface of GCE and dried in air before use. Here, N-doped AGA/GNs remains its original structure (shown in **Fig.s1**). In the study, electrochemical experiment was carried out under room temperature, and all experimental solution was degassed by nitrogen for at least 15 min. Then, a nitrogen atmosphere was maintained during electrochemical measurements.

3 Results and discussion

3.1 Materials synthesis

The N-doped AGA/GNs was synthesized through self-assembly of GO sheets, freeze-drying of GO hydrogel, thermal annealing of GO aerogel and hybridization of N-doped AGA with GNs (shown in **Fig.1**). First, the mixture of graphite oxide, KOH, urea and 2,4,6-trihydroxybenzaldehyde were dispersed in water by ultrasonication to form homogeneous GO dispersion. The dispersion was subsequently heated to form GO hydrogel by hydrothermal method. During the process, GO nanosheets were partly reduced and self-assembled into the GO hydrogel. To decrease the reaction teperature and time for fomation of GO hydrogel, 2,4,6-trihydroxybenzaldehyde was also used as an effective agent for reducing GO in the study. The result shows that in the presence of 2,4,6-trihydroxybenzaldehyde the dispersion turned to black when heated at 90℃for 10 min. After being heated for 1 h, a black monolith formed and slightly floated up to the top of the vial. When prolonging the reaction time to 6 h, the monolith further shrunk and totally separated

with the clear solution at the bottom. This is because the hydrophobic reduced GO tend to assemble into three-dimensional macroscopic structure through p–p interactions and finally form grapheme oxide hydrogel. The fact also demonstrates that 2,4,6-trihydroxybenzaldehyde can assist self-assembly of grapheme oxide sheets into the three-dimensional architectures. Moreover, 2,4,6-trihydroxybenzaldehyde and urea used can cross-link with GO sheets by the chemical bonds, serveing to reinforce three-dimensional framework of graphene oxide hydrogel. Next, the hydrogel was dried by the freeze-drying to form the GO aerogel. Due to slow evaporation of water, high mechanical strength and three-dimensional structure of the hydrogel can be well maintained during the drying. Next, the aerogel was reduced by the thermal annealing in Ar/H_2 environment. Such a simple thermal treatment process achieves the reduction, activation and doping nitrogen of grapheme oxide. Here, the alkali activation was used to fabricate porosity on the surface of carbon materials.[22] The activation of carbon with KOH proceeds as following chemical reactions: $6KOH+C \rightarrow 2K+3H_2+2K_2CO_3$, followed by the decomposition of K_2CO_3 and/or reaction of $K/K_2CO_3/CO_2$ with carbon.[23] Thus, the KOH activation will generate large nanoscale pores on the wall of graphene aerogel.[16] Final, the N-doped AGA was hybridizated with GNs by immersing it in the above GN solution to prepare N-doped AGA/GNs. Owing to strong adsorption capacity, the GN solution was rapidly sucked into the N-doped AGA. The process can be completed within 2 min. Moreover, a freeze-drying was also empolyed for drying of the hybrid to avoid the destruction of three-dimensional structure and the GNs fall off from the surface of N-doped AGA.

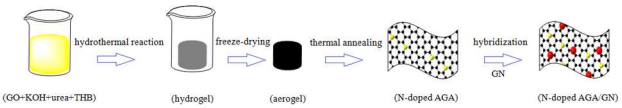

Fig.1 General procedure for the preparation of N-doped AGA/GNs

The SEM, enlarged SEM and TEM images, Raman spectrum and IR spectrum of N-doped AGA were shown in **Fig.s2.** The N-doped AGA displays a rather thin, well-defined, and interconnected three-dimensional network microstructure with uniformly dispersed pores of several micrometers in diameter, suggesting efficient assembly of GO sheets during the hydrothermal reaction (Fig.s2a). The graphene sheets exist the pore of about 20 nm (Fig.s2b). The entire microstructure is composed of very small pores, of order of ~1 nm in size (Fig.s2c). These results also demonstrated that the activation process etches the graphene sheets and generated a three-dimensional distribution of what are referred to as meso- and micropores in the graphene aerogel. The KOH activation yields a continuous three-dimensional network of pores of extremely small size, ranging from 1nm to 20 nm. Thus, it appears that the chemical activation is not merely digesting graphene sheets but also dramatically restructuring it. Raman spectrum is a non-destructive approach to characterize graphitic materials, in particular to determine ordered and disordered crystal structures of graphene. Usually, Raman spectrum of the graphene is characterized by two main features: G band arising from the first order scattering of the E_{1g} phonon of sp^2 carbon atoms and D band arising from a breathing mode of point photons of A_{1g} symmetry.[21] On the Raman spectrum of N-doped AGA, there are two typical Raman peaks of graphene materials, including D band (1320 cm^{-1}) and G band (1591cm^{-1}). Moreover, a high I_D/I_G intensity ratio (1.64) for the N-doped AGA was also obtained in the Fig.s2d, indicating a decrease in the size of the in-plane sp^2 domains and the removal of the oxygen functional groups in the reduced graphene oxide during the thermal annealing, which is consistent with the IR results. Fig.s2e shows that the IR spectrum of N-doped AGA between 600 cm^{-1} and 3900 cm^{-1} appears as an ideal beeline, and characteristic IR absorption peaks of GO and the hydrogel completely disappear. The above results confirm that we have obtained fully exfoliated, reduced and activated N-doped AGA.

C_{1s} and N_{1s} XPS spectra of the N-doped AGA were shown in **Fig.s3.** There are five peaks on the C_{1s} XPS spectrum. The peaks located at 284.4, 286.6 and 288.1eV can be assigned to C-C, C-O and C=O species, respectively.[25] The XPS peak at 285 eV can be assigned to sp^2 C bonded to N. The peak at 288.8 eV can be assigned to O=C–O species. Since the binding energy of an element is related to its chemical environment in a material, the binding energy of the element will move to low energy position when the chemical environment of an element changes from a strong electron withdrawing environment to a relative low one. The peak at 287.7 eV can be assigned to the sp^3 C bonded to N, since the electronegative value of nitrogen is smaller than that of oxygen. On the N_{1s} XPS spectrum, the peak at 398.4 eV can be assigned to N2, corresponds to pyridinic N. The peak at 399.8 eV can be assigned to amide, amine or pyrrolic N. The peak at 401eV can be assigned to N4 and corresponds to graphitic N, indicating that nitrogen replaced the carbon in the graphene sheets and was incorporated into the carbon network.[26] It was noteworthy that the peak intensity of graphitic nitrogen was weaker than that of pyridinic nitrogen and pyrrolic/pyridinic nitrogen, implying that pyridinic nitrogen and pyrrolic nitrogen were dominant in the as-prepared materials. The pyridinic and pyrrolic nitrogen located at the edge of the carbon materials induced more disorders of the final carbon materials, well elucidating the phenomena for the broad D band in Raman spectrum. These results confirmed that the thermal annealing achieved an appropriate nitrogen doping.

3.2 Structure characterization

The SEM, TEM and XRD patterns of N-doped AGA/GNs were shown in **Fig.s4**. From Fig.s4, we observe that GNs are very regular and well dispersed on the wrinkled graphene sheets with an average particle size of about 10 nm. There are four sharp diffraction peaks on the XRD pattern at scattering angles of 38.28°, 44.48°, 64.6° and 77.64°, corresponding to crystal planes Au (111), Au (200), Au (220) and Au (311) of gold face-centered cubic crystallographic structure (JCPDS card No. 65-2870). Moreover, we noted that the GNs were well anchored on the surface of the wall in the aerogel rather than enwraped by the graphene sheets. This could offer more abundant active sites

for the catalytic reduction events and result in the increase of sensitivity for the detection of HQ and DHB.

State-of-the-art surface and pore-size characterization of the N-doped AGA/GNs were performed by nitrogen adsorption/desorption experiments with advanced methods based on the density functional theory. In addition, CO_2 adsorption at 273 K has been performed to assess the ultra micropores. The type IV nitrogen adsorption/desorption isotherm of N-doped AGA/GNs shows a hysteresis loop at high relative pressure (shown in **Fig.2**A), indicating the existence of plentiful mesopores in the aerogel. According to the NLDFT method, the pore size distribution has two sharp peaks at 0.6 nm and 0.8 nm and a broad peak at 2 nm (shown in Fig.2B). The broad pore size distribution, spanning from several to 100 nm, implies that the aerogel is rich in hierarchical pores. Here, the macropores could originate from the interconnected hollow space, the mesopores could be generated by the wrinkled morphology of graphene sheets, and micropores could attribute to the KOH activation. It is noteworthy that the BET surface area for N-doped AGA is up to 1258 m^2 g^{-1}. As far as we know, the specific surface area is the highest value for graphene aerogels reported in literatues,[27] which will largely improve the mass transfer between the electrolyte and the electrode.

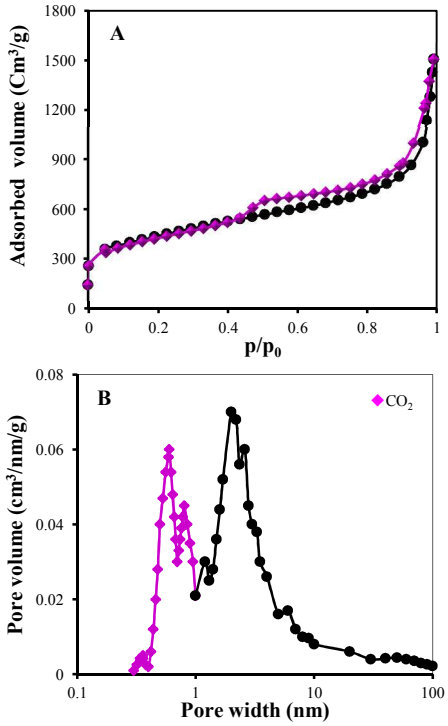

Fig.2 Nitrogen adsorption/desorption isotherm (A) and pore-size distribution curve for N_2 and CO_2 (B) of the N-doped AGA/GNs

Electronic conductivity of N-doped AGA/GNs was determined via the four-probe method. The current was passed through metal electrodes attached to either end of N-doped AGA/GNs, and the voltage drop was measured over distances of 3~6 mm along the aerogel. The bulk electronic conductivity of N-doped AGA/GNs was determined to be 2.8×10^3 S m^{-1}, which is much better than that of other grphene aerogel materials reported in literatures.[28]

3.3 Electrochemical property

To study on electrocatalytic activity of N-doped AGA/GNs, the sensor based on the N-doped AGA/GNs was fabricated and its cyclic voltammetric behavior was investigated in pH 7.0 PBS in 1.0 mM $[Fe(CN)_6]^{3-/4-}$ solution at the scan rate of 100 mV s^{-1}. **Fig.s5** shows that the CV curve of the bare GCE offers well-defined reversible redox behavior attributed to highly electron-transfer between $[Fe(CN)_6]^{3-/4-}$ solution and the electrode. After attachment of the common graphene film on the surface of the electrode, the magnitude of current largely increases, indicating faster electron transfer between $[Fe(CN)_6]^{3-/4-}$ and the electrode, and the reduction potential is shifted towards the higher side at 0.211V as compared to that of bare GCE (0.197V). It appears the graphene enhances electron conduction pathway due to good electronic conductivity. After the graphene was replaced by the activated graphene aerogel, the magnitude of current of the sensor in the CV curve will further increase as compared to that of the sensor based on the common graphene. This should be attributed that the well-defined hierarchical porous structure reduces the mass transfer resistance and enhances the mass transfer of $[Fe(CN)_6]^{3-/4-}$ solution to the electrode. Moreover, we also observed that both nitrogen-doped and gold nanoparticles can increase the magnitude of current of the sensors. In particular, synergistic electrocatalytic properties of the nitrogen-doped, hierarchical porous structure and gold nanoparticles lead to lowering of peak potentials with enhancement in the peak current for the sensor, this would improve the selectivity and sensitivity of the sensor.

The effect of varying scan rate on the performance of the sensor was studied in a pH 7.0 PBS containing 1.0 mM of $K_4Fe(CN)_6$ in 0.1 M KCl. **Fig.3**A exhibits that all scan rates resulted in well-defined reduction and oxidation peaks with little shift in both cathodic and anodic peak potentials with respect to scan rate. Both cathodic and anodic peak currents are linearly proportional with the scan rate square root as shown in Fig.3B, indicating that electrode reaction corresponds to the solution phase is a quasi-reversible process. According to the results of CV, the apparent heterogeneous electron transfer for $Fe(CN)_6^{4-}$ within the N-doped AGA/GNs film was estimated by Laviron's model. Fig.3C presents the relationship plot of peak-to-peak separation value (ΔE_p) with logarithm values of scan rate (logv). A small ΔE_p for all scan rates was observed, indicating fast electron transfer rate. Because the $n\Delta E_p$ is lower than 200 mV, the apparent heterogeneous electron transfer rate constant (k_s) is estimated by the equation (1): [29]

$$k_s = \frac{mnFv}{RT} \qquad (1)$$

where m is a parameter related to peak-to-peak separation; T is the temperature; n is the number of electrons; and v is the scan rate. The k_s was found to be 40.78 ± 0.15 cm s^{-1} and the value is obviously better than that of the bare GCE (5.76±0.33 cm s^{-1}), indicating fast electron transfer of $Fe(CN)_6^{4-}$ solution to the electrode, which would lead to remarkably improve the sensitivity.

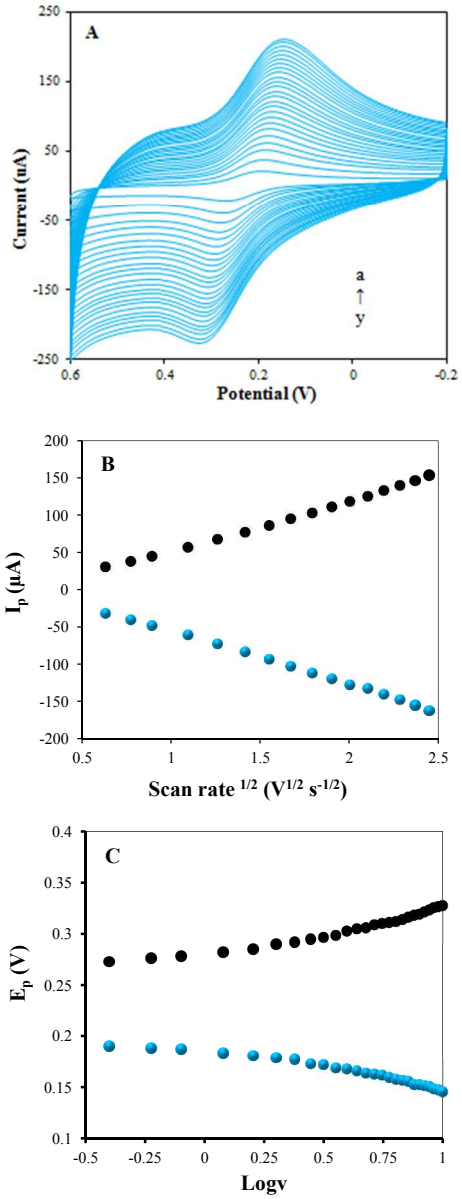

Fig.3 Cyclic voltammograms of the sensor in pH 7.0 PBS containing 1 mM of $K_4Fe(CN)_6$ in 0.1 M KCl at various scan rates (from a to y) of 0.6, 1, 1.2, 1.6, 2.0, 2.4, 2.8, 3.2, 3.6, 4.0, 4.4, 4.8, 5.2, 5.6, 6.0, 6.4, 6.8, 7.2, 7.6, 8.0, 8.4, 8.8, 9.2, 9.6 and 10 V s^{-1}(A), plot of the I_p vs. square root of scan rate (B) and plot of the E_p vs. logv (C)

3.4 Electrocatalytic behavior of HQ and DHB

The electrochemical behaviors of HQ and DHB were studied at the bare GCE and the sensor by cyclic voltammetry. **Fig.4**A presents typical CV curves of the bare GCE and the sensor in pH 7.0 PBS containing 5×10^{-5} M of HQ and 5×10^{-5} M of DHB. For the bare GCE, the oxidation peak potential and the reduction peak of HQ and DHB appear at about 0.356/0.0 and 0.356/0.109 V, respectively. The respective large peak potential separation (ΔE_p) for the HQ and the DHB are 369 and 365 mV, indicating that both HQ and DHB exhibit irreversible electrochemical behavior at the bare GCE. For the sensor, the anodic and cathodic peaks for HQ and DHB are 0.244/0.204 and 0.141/0.094 V, respectively. The reduced ΔE_p of only 40 and 47 mV for the HQ and the DHB manifests the fast electron transfer between HQ (or DHB). Moreover, we also noted that the peak currents also increase more than 18-fold at the sensor. The results demonstrate that the N-doped AGA/GNs lower the oxidation overpotential of HQ and DHB, and thus greatly improved electrochemical reversibility of HQ and DHB. Further, Fig. 4A also reveals that electrochemical response of the sensor to RC is very weak. The fact reveals that a certain concentration of RC did not interfere with the electrochemical detection of HQ and DHB. However, the current peaks in CV curves of HQ and DHB exist some overlap, which may lead to mutual interference for the detection of HQ and DHB. To resolve the problem, we investigated DPV behavior of the sensor in pH 7.0 PBS containing 5×10^{-5} M of HQ, 5×10^{-5} M of DHB and 5×10^{-5} M of RC. Fig.4B shows that DPV curve of the RC is almost a straight line with any current peak, which demonstrates that the RC don't interfere with the detection of HQ and DHB by using the DPV. However, the DPV curves of HQ and DHB have sensitive current peaks. Most importantly, the separation of current peaks between HQ and DHB arrives at about 104 mV, which is large enough to separation the two components. Because the DPV has higher current sensitivity and better resolution than CV, the DPV is selected for the detection of HQ and DHB.

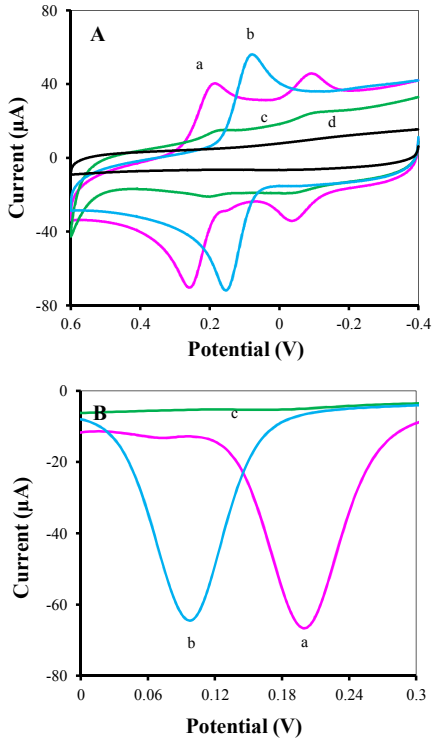

Fig.4 CVs (A) and DPVs (B) of the sensor in pH 7.0 PBS containing 5.0×10^{-5} DHB (a) HQ (b) or RC (c) and bare GCE in pH 7.0 containing 5.0×10^{-5} M of DHB and 5.0×10^{-5} M of HQ (d). The DPV parameters were set to a scan rate of 4 mV/s, 50 mV pulse amplitude, 20 ms pulse width and -0.2 V initial potential

3.5 Analytical characteristics

The representative DPV curves of the sensor in the PBS containing different concentration of HQ and DHB were shown in **Fig.5**. It can be seen that the peak current (I_p) is linear to the

concentration of HQ in the range of 5×10^{-8}-1.8×10^{-4} M. The corresponding linear regression equations is expressed in the following equation: I_p=-0.3289C-10.508, with statistically significant correlation coefficient of 0.9977, where I_p is the DPV peak current in μA and C is the concentration of HQ in the unit of μM; The I_p is linear to the concentration of DHB in the range of 1.0×10^{-8}-2.0×10^{-4} M. The corresponding linear regression equations is expressed in the following equation: I_p=-0.4071C-8.6043, with statistically significant correlation coefficient of 0.9986, where I_p is the DPV peak current in μA and C is the concentration of DHB in the unit of μM. The detection limit is 1.5×10^{-8} M for HQ and 3.3×10^{-9} M for DHB that were obtained from the signal-to-noise characteristics of these data (S/N=3). The sensitivity is obviously better than that of other sensors based on the other graphene materials such as (4-ferrocenylethyne)phenylamine carbon nanoparticles/ graphene (1.0×10^{-7} M for HQ and 7.0×10^{-7} M for DHB),[30] graphene/polymer composite (2.0×10^{-4} M for HQ)[31] and poly(diallyl-dimethylammonium chloride) functionalized graphene (2.5×10^{-7} M for HQ and 2.0×10^{-7} M for DHB).[32]

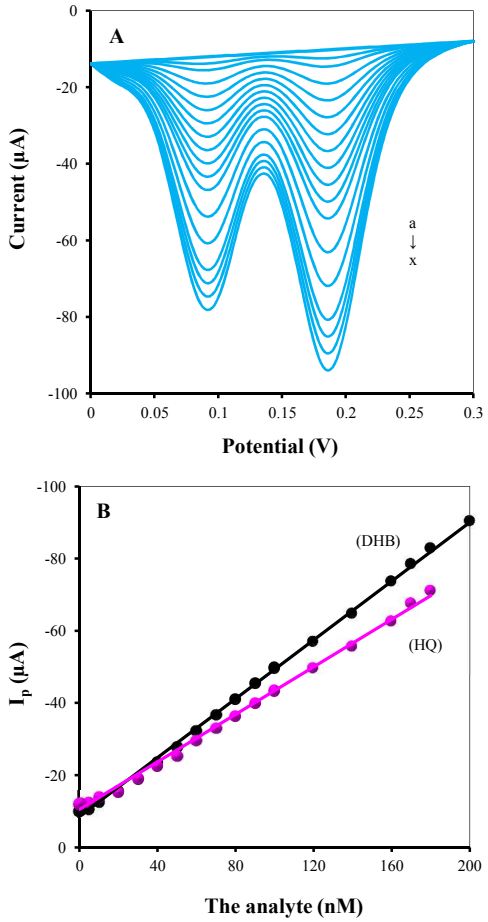

Fig.5A: DPVs of the sensor in PBS containing 0.0, 1×10^{-8}, 5×10^{-8}, 1×10^{-7}, 5×10^{-7}, 1.0×10^{-6}, 5×10^{-6}, 1.0×10^{-5}, 2.0×10^{-5}, 3.0×10^{-5}, 4.0×10^{-5}, 5.0×10^{-5}, 6.0×10^{-5}, 7.0×10^{-5}, 8.0×10^{-5}, 9.0×10^{-5}, 1.0×10^{-4}, 1.2×10^{-4},1.4×10^{-4}, 1.6×10^{-4}, 1.7×10^{-4}, 1.8×10^{-4}, 2.0×10^{-4} and 2.2×10^{-4} DHB and HQ (from a to x)(A). B: calibration plots of concentration of DHB and HQ vs. peak current change (ΔI_p). The DPV parameters were set to a scan rate of 4 mV/s, 50 mV pulse amplitude, 20 ms pulse width and -0.2 v initial potential

Relative standard deviation (RSD%) of the sensor in successive eleven scans for HQ and DHB are 0.17% and 0.23%, respectively. Twenty sensors were prepared independently under the same operating conditions, revealing an acceptable reproducibility with RSD 2.1% and 1.9% for HQ and DHB. Finally, the stability of modified electrode was examined by storing it in a place at 4℃ for four weeks. The peak current remained 96.2% of originally measured value. These results confirm excellent reproducibility and stability.

The possible interferences of some species on the simultaneous determination of HQ and DHB were studied by DPV detection. The results showed that there are no significant interference from many common cations and anions in real water sample, including 1000-fold Na(I), K(I), NH_4(I), Ca(II), Mg(II), Zn(II), Al(III), F^-, Cl^-, Br^-, NO_3^-, SO_4^{2-}, CO_3^{2-}, 50-fold Fe(III), Cu(II) and I^-, 10-fold glucose, ascorbic acid and uric acid, and 5-fold RC don't interfere the determination. The tolerance limit was estimated to be less than 4.6% of the relative error, indicating a high anti-interference ability.

3.6 Comparison of different materials

To evaluate role of the each innovative element in the study, a series of graphene materials were designed and synthesized in the laboratory. For each sample, its elemental composition, particle size distribution of GNs and properties were investigated in detail. Based on comprehensive analysis of the results listed in Table s1, Fig.s6 and Table 1, we can draw four conclusions. The first conclusion is that the activated graphene/gold offers the highest BET surface area, which is more than 8-fold that of the graphene/gold. The fact confirms that the KOH activation is a powerful tool for increasing the specific surface area of graphene materials. The bigger surface area will result in fuller contact between the electrolyte and electrode material. Thus, the k_s value of activated graphene/gold is up to 26.8 cm s^{-1}. However, electronic conductivity (EC) of the activated graphene/gold is slightly lower than that of the graphene/gold. This is because the KOH activation produces a large number of micropores on the surface of graphene sheets, that destroys the integrity of the electron conjugated system of graphene sheets and results in the decrease of the activated graphene/gold. The second conclusion is that electronic conductivity of the activated graphene aerogel/gold is obviously higher than that of the activated graphene/gold, which is more than 5-fold that of the activated graphene/gold. Because AGA/GNs and AG/GNs have almost same carbon, oxygen and gold contents as well as particle size distribution of GNs, such a remarkable improvement in the electronic conductivity should be attributed that graphene sheets interconnected to form three-dimensional conductive network in the aerogel. Moreover, the high electronic conductivity will further improve the heterogeneous electron transfer. The third conclusion is that k_s value of the N-doped AGA/GNs is more than that of the activated graphene aerogel/gold, indicating that the nitrogen doping further improves the contact between the electrolyte and the electrode materials. This is because the nitrogen atom types doped in the N-doped AGA/GNs mainly are pyridinic nitrogen and pyrrolic nitrogen, which were located at the edge of the carbon materials

induced more disorders of the final carbon materials. Thus, the doping nitrogen will increase the adsorption ability of the electrolyte ions such as $Fe(CN)_6^{4-/3-}$, HQ and DHB on the surface of graphene aerogel. This is beneficial to fully contact between the electrolyte and the material, and result in an increase of the k_s value. The fourth conclusion is that both GNs and N-doped AGA can offer obvious electrocatalytic activity towards HQ. However, the sensors based on the N-doped AGA and GNs have a lower sensitivity for detection of HQ when compared with the sensor based on the N-doped AGA/GNs, indicating that the combination of N-doped AGA with GNs leads to an largely enhanced electrocatalytic activity. Therefore, we think that high sensitivity and fast electrochemical response of the proposed sensor should be attributed to excellent electron transfer and mass transport of N-doped AGA/GNs as well as the remarkable synergistic electrocatalytic effect between N-doped AGA and GNs.

Table 1 The properties of different materials

Material	BET (m2 g-1)	EC (S m-1)	ks (cm s-1)	DL (HQ) (M)
graphene/gold nanoparticles (G/GNs)	325	5.2×10^{2}	13.2	-
activated graphene/gold (AG/GNs)	2623	5.0×10^{2}	26.8	-
activated graphene aerogel/gold (AGA/GNs)	1468	2.1×10^{3}	35.2	-
nitrogen-doped activated graphene aerogel/gold (N-doped AGA/GNs)	1258	2.8×10^{3}	40.78	1.5×10^{-8}
nitrogen-doped activated graphene aerogel (N-doped AGA)	-	-		1.9×10^{-4}
gold nanoparticles (GNs)	-	-	-	3.5×10^{-3}

3.7 Sample analysis

The feasibility of the newly developed method for possible applications was investigated by analyzing real water samples. All water samples including surface water, ground water and industrial waste were collected from the factory for producing HQ and DHB located in China. The spike and recovery experiments were performed by measuring the DPV responses to the sample in which the known concentrations of HQ and DHB were added. The concentration of HQ and DHB in water sample was determined from the calibration curve and the value was used to calculate the concentration in the original sample. The mean ± SD of each sample and recovery of each spiked sample were calculated, and the values are reported in **Table 2**. The recovery of HQ and DHB for spiked samples analysis is in the range of 96.8-103.2%. These indicated proposed method has a good accuracy and precision.

Table 2 The results for detection of HQ and DHB in water samples (N=5)

Sample	Surface water		Ground water		Industrial waste	
	HQ	DHB	HQ	DHB	HQ	DHB
added (μM)	0.5	0.5	0.5	0.5	0.5	0.5
determined (μM)	0.22±0.05	0.16±0.05	1.68±0.11	0.80±0.06	3.06±0.27	1.63±0.12
RSD (%)	1.4	1.1	1.8	1.2	1.7	1.1
Recovery (%)	101.5	96.8	103.2	103.1	100.2	102.1

4 Conclusions

The study demonstrated a new strategy for synthesis of N-doped AGA/GNs and its application as a novel sensing material for the electrochemical detection of HQ and DHB. The as-synthesized N-doped AGA/GNs offers an excellent electronic conductivity, large specific surface area, well-defined 3D hierarchical porous structure and fast apparent heterogeneous electron transfer, which are remarkably better than that of present graphene aerogel materials. Owing to the greatly enhanced electron transfer and mass transport, the sensor based on N-doped AGA/GNs displays ultrasensitive electrochemical response to HQ and DHB. The method provides the advantage of sensitivity, repeatability and stability compared with present HQ and DHB sensors. More importantly, the study provides a promising approach for the fabrication of various graphene aerogel materials, which can be potentially applied in biosensor, electrocatalysis and energy storage/conversion device.

Acknowledgments

The authors acknowledge the financial support from the National Natural Science Foundation of China (No.21176101), the Fundamental Research Funds for the Central Universities (No.JUSRP51314B), MOE & SAFEA for the 111 Project (B13025) and the country "12th Five-Year Plan" to support science and technology project (No. 2012BAK08B01).

Notes and references

[a] *School of Chemical and Material Engineering, Jiangnan University, Wuxi, China. Fax:86051085811863; Tel:13912371144; e-mail: zaijunli@263.net*
[b] *The University of Birmingham, Edgbaston, Birmingham, BI5 2TT, United Kingdom*
[c] *Key Laboratory of Food Colloids and Biotechnology, Ministry of Education, Wuxi 214122, China*

† Electronic Supplementary Information (ESI) available: [details of any supplementary information available should be included here]. See DOI: 10.1039/b000000x/

1 S. Nardecchia, D. Carriazo, M.L. Ferrer, M.C. Gutierrez, F.D. Monte, *Chem. Soc. Rev.*, 2013, **42**, 794.
2 Y.X. Xu, Q. Wu, Y.Q. Sun, H. Bai, G.Q. Shi, *ACS Nano*, 2010, **4**, 7358.
3 H. Bai, C. Li, X.L. Wang, G.Q. Shi, *Chem. Commun.*, 2010, **46**, 2376.
4 B. Adhikari, A. Biswas, A. Banerjee, *ACS Appl. Mater. Interfaces*, 2012, **4**, 5472.
5 J. Nanda, A. Biswas, B. Adhikari, A. Banerjee, *Angew. Chem. Int. Ed.*, 2013, **52**, 5041; J. Nanda, A. Biswas, B. Adhikari, A. Banerjee, *Angew. Chem.*, 2013, **125**, 5145; B. Adhikari, A. Biswas, A. Banerjee, *Langmuir*, 2012, **28**, 1460; W.F. Chen, S.R. Li, C.H. Chen, L.F. Yan, *Adv. Mater.*, 2011, **23**, 5679.
6 J.J. Yuan, J.W. Zhu, H.P. Bi, X.Q. Meng, S.M. Liang, L.L. Zhang, X. Wang, *Phys. Chem. Chem. Phys.*, 2013, **15**, 12940.
7 J. Li, F. Wang, C.Y. Liu, *J. Colloid Interf. Sci.*, 2012, **382**, 13.
8 L. Ren, K.S. Hui, K.N. Hui, *J. Mater. Chem. A*, 2013, **1**, 5689.
9 X. Mi, G.B. Huang, W.S. Xie, W. Wang, Y. Liu, J.P. Gao, *Carbon*, 2012, **50**, 4856.
10 Y.Q. He, N.N. Zhang, F. Wu, F.Q. Xu, Y. Liu, J.P. Gao, *Mater. Res. Bull.*, 2013, **48**, 3553.
11 Y.J. Zhong, M. Zhou, F.Q. Huang, T.Q. Lin, D.Y. Wan, *Sol. Energ. Mat. Sol. C.*, 2013, **113**, 195.
12 M.M. Liu, R. Liu, W. Chen, *Biosens. Bioelectron.*, 2013, **45**, 206.

13 W.J. Si, X.Z. Wu, J. Zhou, F.F. Guo, S.P. Zhuo, H.Y. Cui, W. Xing, *Nanoscale Res. Lett.*, 2013, **8**, 247.
14 Z. Han, Z.H. Tang, P. Li, G.Z. Yang, Q.B. Zheng, J.H. Yang, *Nanoscale*, 2013, **5**, 5462.
15 X.Z. Wu, J. Zhou, W. Xing, G.Q. Wang, H.Y. Cui, S.P. Zhuo, Q.Z. Xue, Z.F. Yan, S.Z. Qiao, *J. Mater. Chem*., 2012, **22**, 23186.
16 Y.W. Zhu, S. Murali, M.D. Stoller, K.J. Ganesh, W.W. Cai, P.J. Ferreira, A. Pirkle, R.M. Wallace, K.A. Cychosz, M. Thommes, D. Su, E.A. Stach, R.S. Ruoff, *Science*, 2011, **332**, 1537.
17 H.J. Yin, S.L. Zhao, J.W. Wan, H.J. Tang, L. Chang, L.C. He, H.J. Zhao, Y. Gao, Z.Y. Tang, *Adv. Mater.*, 2013, DOI:10.1002/adma.201302223.
18 H.J. Tang, H.J. Yin, J.Y. Wang, N.L. Yang, D. Wang, Z.Y. Tang, *Angew. Chem. Int. Ed*., 2013, **52**, 5585.
19 H.J. Yin, H.J. Tang, D. Wang, Y. Gao, Z.Y. Tang, *ACS Nano*, 2012, **6**, 8288.
20 Q.F. Cheng, M.X. Wu, M.Z. Li, L. Jiang, Z.Y. Tang, *Angew. Chem. Int. Ed.*, 2013, **52**, 3750.
21 W.S. Hummers, R.E. Offeman, *J. Am. Chem. Soc*., 1958, **80**, 1339.
22 V. Barranco, M.A. Lillo-Rodenas, A. Linares-Solano, *J. Phys. Chem. C*, 2010,**114**, 10302; E. Raymundo-Pinero, P. Azais, T. Cacciaguerra, D. Cazorla-Amoros, A. Linares Solano, F. Beguin, *Carbon*, 2005, **43**, 786.
23 Z.S. Wu, W. Ren, L. Wen, L. Gao, J. Zhao, Z. Chen, G. Zhou, F. Li, H.M. Cheng, *ACS Nano*, **2010**, 4, 3187.
24 A.C. Ferrari, J. Robertson, *Phys. Rev. B*, 2000, **61**, 14095.
25. Z.G. Mou, X.Y. Chen, Y.K. Du, X.M. Wang, P. Yang, S.D. Wang, *Appl. Surf. Sci.*, 2011, **258**, 1704.
26 S. Yasuda, L.Yu, J. Kim, K. Murakoshi, *Chem. Commun.*, 2013, **49**, 9627.
27 W.Y. Cheng, C.C. Wang, S.Y. Lu, *Carbon*, 2013, **54**, 291; Z. Fan, D.Z.Y. Tng, S.T. Nguyen, J.D. Feng, C.F. Lin, P.F. Xiao, L. Lu, H.M. Duong, *Chem. Phys. Lett.*, 2013, **561-562**, 92; F.C. Meng, X.T. Zhang, B. Xu, S.F. Yue, H. Guoc, Y.J. Luo, *J. Mater. Chem*., 2011, **21**, 18537.
28 M.X. Chen, C.C. Zhang, X.C. Li, L. Zhang, Y.L. Ma, L. Zhang, X.Y. Xu, F.L. Xia, W. Wang, J.P. Gao, *J. Mater. Chem. A*, 2013,**1**, 2869; Z.Y. Sui, Q.H. Meng, X.T. Zhang, R. Ma, B. Cao, *J. Mater. Chem*, 2012, **22**, 8767; M.A. Worsley, P.J. Pauzauskie, T.Y. Olson, J. Biener, J.H. Satcher, T.T. Baumann, *J. Am. Chem. Soc*., 2010, **132**, 14067.
29 E. Laviron, *J. Electroanal. Chem.*, 1979, **101**, 19.
30 L.P. Wang, Y. Meng, Q. Chen, J.H. Deng, Y.Y. Zhang, H.T. Li, S.Z. Yao, *Electrochim. Acta*, 2013, **92**, 216.
31 Z.L. Zhang, Y.M. Liang, W. Liu, K. Chen, *Sensors*, 2013, **13**, 6204.
32 L.T. Wang, Y. Zhang, Y.L. Du, D.B. Lu, Y.Z. Zhang, C.M. Wang, *J. Solid State Electr.*, 2012, **16**, 1323.